remote sensing

MDPI

Article

Hyper-Temporal C-Band SAR for Baseline Woody Structural Assessments in Deciduous Savannas

Russell Main [1,2,*], Renaud Mathieu [1,2], Waldo Kleynhans [3,4], Konrad Wessels [2,3], Laven Naidoo [1,2] and Gregory P. Asner [5]

1 Ecosystems Earth Observation, Natural Resources and the Environment, CSIR, Pretoria 0001, South Africa; rmathieu@csir.co.za (R.M.); lnaidoo@csir.co.za (L.N.)
2 Department of Geography, Geomatics and Meteorology, University of Pretoria, Pretoria 0028, South Africa; kwessels@csir.co.za
3 Remote Sensing Research Unit, Meraka Institute, CSIR, Pretoria 0001, South Africa; wkleynhans@csir.co.za
4 Department of Electrical, Electronic and Computer Engineering, University of Pretoria, Pretoria 0001, South Africa
5 Department of Global Ecology, Carnegie Institution for Science, Stanford, CA 94305, USA; gpa@carnegiescience.edu
* Correspondence: rmain@csir.co.za; Tel.: +27-841-3840

Academic Editors: Randolph H. Wynne and Prasad S. Thenkabail
Received: 28 June 2016; Accepted: 3 August 2016; Published: 17 August 2016

Abstract: Savanna ecosystems and their woody vegetation provide valuable resources and ecosystem services. Locally calibrated and cost effective estimates of these resources are required in order to satisfy commitments to monitor and manage change within them. Baseline maps of woody resources are important for analyzing change over time. Freely available, and highly repetitive, C-band data has the potential to be a viable alternative to high-resolution commercial SAR imagery (e.g., RADARSAT-2, ALOS2) in generating large-scale woody resources maps. Using airborne LiDAR as calibration, we investigated the relationships between hyper-temporal C-band ASAR data and woody structural parameters, namely total canopy cover (TCC) and total canopy volume (TCV), in a deciduous savanna environment. Results showed that: the temporal filter reduced image variance; the random forest model out-performed the linear model; while the TCV metric consistently showed marginally higher accuracies than the TCC metric. Combinations of between 6 and 10 images could produce results comparable to high resolution commercial (C- & L-band) SAR imagery. The approach showed promise for producing a regional scale, locally calibrated, baseline maps for the management of deciduous savanna resources, and lay a foundation for monitoring using time series of data from newer C-band SAR sensors (e.g., Sentinel1).

Keywords: SAR; ASAR; hyper-temporal; C-band; canopy cover; canopy volume; savanna

1. Introduction

Savanna ecosystems are ecologically and economically significant systems that are defined by a continuous herbaceous layer interspersed with trees [1,2]. They cover more than 30% of the worlds' vegetated land surface, and more than half of the African continent, thereby providing millions of mostly poorer households with materials (e.g., grazing resource, timber, fuelwood, edible fruits and roots) they need in order to buffer the full effects of poverty [3,4]. Savannas have great carbon sequestration potential within the global carbon cycle [5], and are either facing high levels of utilization through harvesting [6], or bush encroachment threatens the availability of viable grazing land [7,8]. The (potential) impacts of these combined pressures on woody resources in (African) savannas need to be monitored in order to avoid significant losses, both in terms of ecosystem services, as well as

associated livelihoods. This requires being able to accurately measure, report, and verify available woody resources in order that they are sustainably managed.

To date in southern Africa, the most up-to-date information of this kind is in the form of global products, which are poorly calibrated outside of boreal and tropical forest environments. Apart from having a responsibility to their citizens for the monitoring of these resources, governments have additional legal obligation through the signing of international treaties (e.g., Kyoto protocol, United Nations Convention to Combat Desertification, FAO Forest Resource Assessment), or the promulgation of national acts and strategic initiatives. However, there are no regularly updated national spatial products or datasets, regarding the status or trends in South(ern) Africa's woodland and forest resources.

Space-borne synthetic aperture radar (SAR) data are an ideal data source to map forest attributes given that: (a) SAR systems are active (microwave) remote sensing systems, which operate at low frequencies that result in microwaves penetrating the canopy and (b) SAR systems have the ability to capture data despite the presence of cloud cover, fog, smoke, or dust [9,10]. SAR remote sensing operates on the premise that the microwaves interact with the structural and dielectric (i.e., water content) properties of tree elements, as a function of the SAR frequency [11]. Longer SAR wavelengths, such as L-band (~23.9 cm) and P-band (~68 cm), are able to penetrate further into vegetation canopies than shorter wavelengths, such as the X-band (~3.1 cm) and C-band (~5.6 cm). Hence, longer SAR wavelengths have been shown to be particularly successful in extracting forest parameters when used in dense forested environments [12,13], as well as open forests such as savannas [14,15]. Research has also been conducted into S-band (~10 cm) SAR and its interactions with vegetation parameters [16]. The shorter wavelengths tend to interact more with small branches and twigs in the upper layers of the canopy, instead of the larger branches and trunk of the tree where the majority of the biomass is stored [17]. Studies have shown however, that shorter wavelength SAR data are capable of producing useful relationships with vegetation parameters when using interferometric or physical based SAR methods [18,19]. Recently, in Southern African savannas [20] conducted a multi-frequency investigation and concluded that single L-band imagery was more effective in estimating woody canopy cover, canopy volume, and above ground biomass when compared to single date C- or X-band data. The southern African savanna woodlands (i.e., open forests or canopy) are typically a mixture of grass, dispersed tall trees, as well as clumps of multi-stemmed shrubs and smaller trees that have coppiced due to disturbance events (i.e., fire, herbivore browsing, harvesting). The short (e.g., ~3–5 m) multi-stemmed clumps can comprise a significant portion of the woody cover within a region, especially in areas where fuel wood harvesting is prevalent. Studies such as [14] in the woodlands of Queensland (AIRSAR), Australia, and [21] in a South African savanna (RADARSAT-2), showed that open canopy environments may favor a higher penetration of short microwaves within the canopy profiles and enhance the effectiveness of C-band imagery to retrieve woody parameters. Whereas the aforementioned studies used high resolution commercial SAR sensors (e.g., RADARSAT2, ALOS PALSAR, TerraSAR-X), there remains a need to establish the estimation protocols necessary for woody parameter assessments using routinely available, and free, SAR backscatter data. To date, C-band data remains the only freely available and systematically collected SAR datasets available. These include, the ENVISAT ASAR archive data (2006–2011), and for ensuring temporal continuity the data from the ESA Sentinel-1a and 1b satellites, which were launched in 2014 and 2016 respectively.

Multi-date SAR imagery is used to improve discrimination of land cover classes and strengthen classification efforts [22], as well as to increase the contribution of vegetation-related backscatter and thereby reduce the noise originating from environmental sources [23]. The advantages of temporal SAR data over single image data have been successfully demonstrated in a number of environments, such as boreal forests [24–26], wetlands [27], and Indian deciduous moist forests [28]. It is postulated in this study that a time series of ENVISAT ASAR backscatter data can be used to produce locally-calibrated baseline woody structure products across extensive savanna landscapes. These, ASAR-derived, historical baseline products could then act as points of departure for change assessments using

the European Space Agency's (ESA) Copernicus mission and its SAR C-band sensor (Sentinel-1). In addition, having access to precision LiDAR data that coincides with the acquisition of SAR data is rare (especially in African savanna regions), and thereby provides an excellent opportunity to investigate the woody parameter estimation abilities of a time series of archive, medium resolution, C-band SAR images. In the absence of above ground biomass data that coincided with the SAR data, the following woody parameters were calculated from the LiDAR data; the total canopy cover (TCC), and total canopy volume (TCV). The TCC represents the percentage area occupied by woody canopies. The TVC represents the total volume of vegetation material within a vertical profile. Both metrics adequately describe aspects of the vegetation structure within savanna environments, and both have previously shown good relationships with SAR backscatter data [20,21].

The aims of the study were to assess; (a) the strength of the relationships between savanna woody vegetation cover and volume and a time-series of C-band ASAR data using empirical modelling; and (b) the effect that image filtering, rainfall and seasonality, and/or number of images, have on those relationships. The study explored the ASAR data and TCC and TCV relationships under different scenarios comprising images that were (a) unfiltered or temporally filtered; (b) combinations of single or multiple phenological cycles; or (c) split into wet (leaf-on), dry (leaf-off), or both wet and dry periods. A truly hyper-temporal (i.e., more than 10 images) approach to woody parameter estimation, using medium resolution C-band SAR, has not yet been investigated in an (African) savanna environment. It is hypothesized that the hyper-temporal time series of SAR data will compensate for the challenges posed by the shorter SAR wavelength, the lower spatial resolution (75 m), and the spatial variability within the landscape, in order to successfully model woody structural parameters within this environment.

2. Study Area

The study area is situated in the Lowveld region of the savanna biome at the north-eastern edge of South Africa (Figure 1). The region is primarily made up of three different land uses, namely communal rangelands within the Bushbuckridge Municipality (BBR), private game reserves (e.g., Sabi Sands Game Reserve), as well as state owned conservation in the form of the Kruger National Park. Each of the three land uses border one another at some point within the region, and each has very different vegetation management styles. The winters in the region are short and dry, while the summer rains occur between October and May across a rainfall gradient that can vary from 250 mm/annum in the East to 1000 mm/annum in the West. In combination with this rainfall gradient, the vegetation distribution and density are also influenced by geology, fire events, mega-herbivore browsing, cattle grazing, and anthropogenic harvesting of woody vegetation. The vegetation type is considered a mixture of Clay Thornbush, Mixed Bushveld, and Sweet and Sour Lowveld Bushveld [29]. Coppicing of the vegetation is prominent in the area, particularly in areas that experience high levels of anthropogenic utilization. The woody canopy cover can range from 5% in the open savanna, to 60% in woodland areas, and 80% in riparian areas [30].

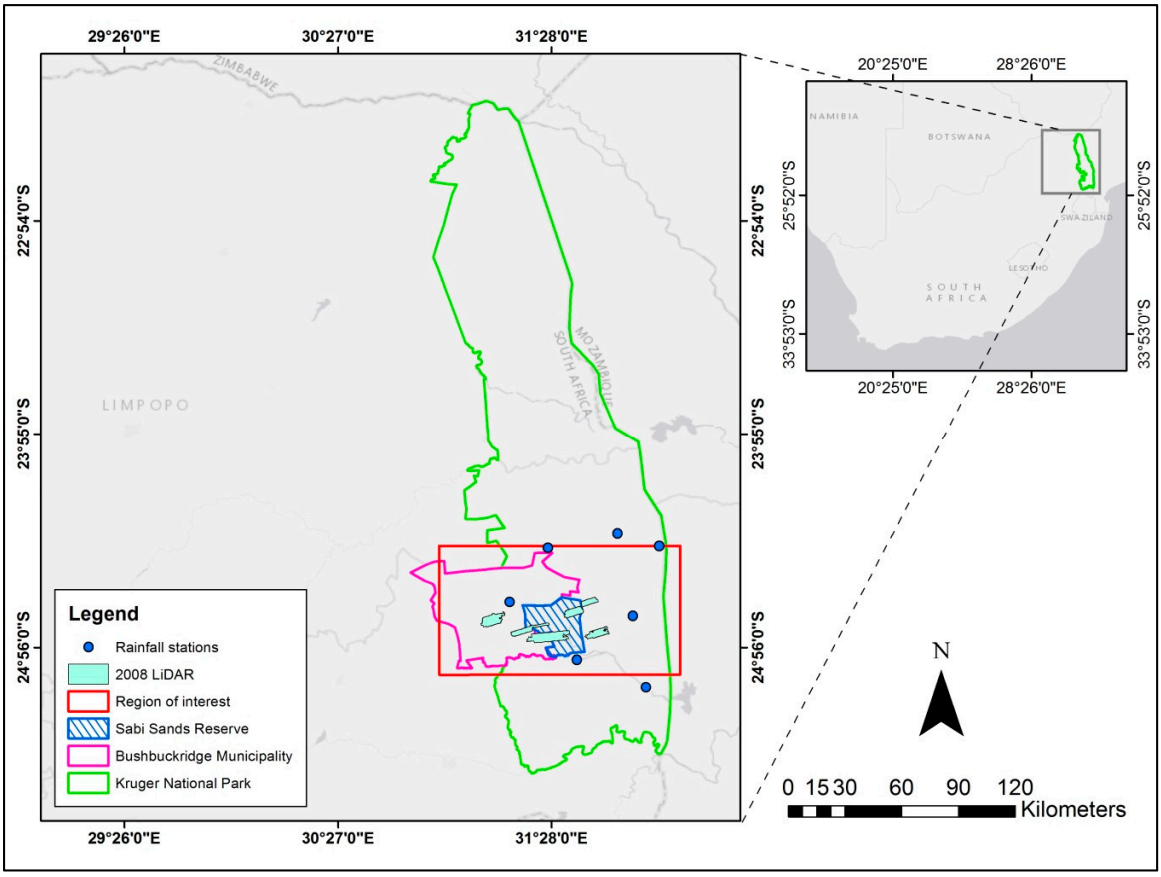

Figure 1. Study area map of the Lowveld region of South Africa, with three land uses (i.e., Sabi Sands private nature reserve, Bushbuskridge communal rangelands, and the Kruger National Park), the LiDAR acquisitions, rainfall stations, and region of interest displayed.

3. Materials and Methods

3.1. Remote Sensing Data

The hyper-temporal SAR data consisted of 43 irregularly timed ENVISAT ASAR wide-swath mode (WSM_1P) HH polarization images, which were acquired between December 2006 and December 2009. The images were in ground range resolution format (e.g., 75 m range & azimuth pixel spacing), and only images that fully covered the region of interest were included. Only the HH polarized images were used, as there was a denser time series compared to VV polarized images, and because the HH polarization has been shown to achieve better accuracies for woody vegetation [17,21]. The 43 HH co-polarized images were classified into 17 wet (November to April) and 26 dry (May to October) period images. The 43 available images spanned three phenological cycles, i.e., images between October (start of greening season) and September (end of dry season) for each of the 2006/2007, 2007/2008, and 2008/2009 cycles. The images were split into different scenarios, including combinations of wet (W) and/or dry (D) images for each phenological cycle. The mean incidence angle across the study area for each cycle was; (i) 32° (Min: 19.6°, Max: 42°) for the 2006/2007 cycle; (ii) 31.3° (Min: 19.6°, Max: 42°) for the 2007/2008 cycle; and (iii) 31.5° (Min: 15.9°, Max: 42°) for the 2008/2009 cycle.

Each ASAR WSM_1P ground range intensity image was pre-processed using the GAMMA™ radar processing software [31]. We opted to preserve as much spatial detail as possible, and so chose not to conduct further multilooking. The processing steps included the conversion of digital numbers to sigma-nought (σ°) via a radiometric calibration. Calibration factors were extracted from the individual image headers and applied (i.e., 68 dB). The images were then geometrically and topographically

corrected using a 30 m (1 Arc second) Shuttle Radar Topography Mission (SRTM) DEM. The steps included in the geometric and orthorectification process include: (i) generation of look-up tables for each of the SAR geometry and DEM map geometry pixels; (ii) use of the DEM to simulate a SAR intensity image from map geometry to SAR geometry; (iii) co-register the simulated and real SAR images in SAR geometry; (iv) refine the look-up table and geocode the original SAR image into map geometry [31]. The final step involved using the local incidence angle to normalize topographic effects on the backscatter.

The SAR images were temporally filtered, using the Quegan filter described in [32]. This filter linearly combines images of a given time series, and creates a new set of speckle reduced images. The filter uses the input intensity data, as well as a local mean backscattering coefficient that is estimated in a window around each pixel [32]. The filter serves to reduce the variance (i.e., speckle) within the image, while preserving both radiometric and spatial resolution. Three different filter window sizes were tested, namely 3 × 3, 7 × 7, and 11 × 11 pixels. No significant improvement in accuracy was found beyond an 11 × 11 pixel filter window. The temporal filter was applied to the full stack of 43 images in order to maximize the reduction of speckle. We assessed the filters' speckle suppression at the image level, rather than having to identify homogeneous areas in a savanna landscape which is intrinsically heterogeneous. The ratio of the unfiltered image to the filtered image, also called the Speckle Image Statistical Analysis (SISA) index, was used [33]. The SISA index produces an image of speckle, with the mean and standard deviation of this image expressing the filter's ability to retain the original mean values (i.e., closer to 1, the better) and suppress speckle, respectively [34].

Airborne LiDAR data were used to calibrate and validate predictive SAR models for total woody cover (TCC) and total canopy volume (TCV). The LiDAR data totaled approximately 35,000 ha, and was acquired during April–May 2008 using the Carnegie Airborne Observatory (CAO) Alpha system [35]. High resolution canopy height models enabled the calculation of TCC, which is the percentage area that is occupied by woody vegetation, within a 150 m× 150 m grid cell (corresponding to 2 × 2 ASAR pixels). Only vegetation above 1m was considered in deriving the TCC metric, in order to exclude the grassy savanna component, and due to the LiDAR system's limited sensitivity below 1m [36]. Total canopy volume is a metric derived from pseudo waveform LiDAR data, where LiDAR hits are binned into volumetric pixels and weighted relative to the total number of hits within the vertical column [35]. The TCV was calculated from a 5 m × 5 m window (i.e., voxel) at different heights (i.e., 1 m bins/slices) above 1 m, to derive a unitless metric as a proxy for the volume of vegetation within the vertical profile of vegetation (See [21,35] for more detail).

3.2. Ancillary data

SAR backscatter is influenced by environmental factors such as moisture in the landscape, in that the dielectric constant of ground targets changes, which results in increases in backscatter [37]. Episodic precipitation events should therefore be taken into consideration when analyzing time series SAR data. Daily rainfall data was retrieved from several stations in the region, and for the period between September 2006 and December 2010 [38,39]. The daily rainfall data was summed across seven rainfall stations per month, and then used to calculate total rainfall amounts for each of the phenological cycles, as well as each cycle's respective wet and dry periods. The total rainfall in the days prior to image acquisition (i.e., day of, plus one and two days prior) was also calculated. The rainfall occurring in the days just prior to image acquisition is likely to increase the amount of moisture both in the soil and grass as well as on the leaves and twigs of the woody canopies themselves.

3.3. Sampling and Statistical Analysis

The sampling was conducted using a 2 × 2 pixel window (i.e., 150 m × 150 m), spaced 75 m apart, to extract data from each of the LiDAR and SAR datasets. The one pixel (i.e., 75 m) spacing considered a previous geostatistical analysis [36], which showed 50 m to be the distance beyond which no spatial autocorrelation occurs. After extracting the mean values for each dataset (n = 3852)

a Monte Carlo (i.e., leave-group-out) cross validation strategy was followed, with 25 repetitions and a training/validation split of 35%/65%, respectively. The statistical relationships between the woody structure parameters (i.e., TCC and TCV) and the SAR image scenarios were modelled using multi-linear regression (ML) and random forest (RF) models, and were assessed using regression statistics such as the correlation coefficient (R^2), the root mean squared error (RMSE), and the relative root mean squared error (rRMSE). An analysis showed there was little benefit in allowing the RF model to grow beyond 250 trees, or optimize it further than the default parameters. The modelling of these relationships was carried out using the open source R statistical package [40].

4. Results

4.1. Rainfall Effects on Backscatter

We attempted to acknowledge, and understand, the effects of moisture on backscatter by analyzing recorded rainfall data against the measured time series of SAR backscatter values. The variability of the mean (and ± one standard deviation) backscatter profile over the time series is displayed and summarized in Figure 2a–d. The dry season showed a noticeable drop in the backscatter, accompanied by reduced variability, whereas the wet season showed increased backscatter responses to rainfall events and therefore a higher backscatter variability (Figure 2a,d). The 2008/2009 phenological cycle experienced the highest total rainfall (Table 1), and subsequently produced the highest mean backscatter (Figure 2c). The 2007/2008 cycle experienced the least amount of dry period rainfall (Table 1), and coincides with the highest number (12) of dry period images, which also produced the lowest mean backscatter (Figure 2c). As expected, all the dry periods showed lower mean backscatter responses than their respective wet periods, particularly in the case of 2007/2008 and 2008/2009 (Figure 2d). Majority (i.e., 11 out of 17) of the wet season images experienced some rain prior to the image being captured, and many of these subsequently responded with increases in the backscatter response (Figure 2b). The mean coefficient of variation across all stations is high for all three cycles, and can be viewed as an indicator of the spatial and temporal variability of rainfall in the region (Table 1).

Table 1. The total rainfall for each phenological cycle, as well as for each dry and wet period within each cycle. The mean coefficient of variation (%) for each period is presented in brackets. The values were extracted from seven weather stations within the region of study.

Phenological Cycle (October–September)	Total (mm)	Dry–Total (May–September) (mm)	Wet–Total (October–April) (mm)
2006/2007	494.4 *(111.2)*	107.3 *(76.2)*	387.1 *(146.2)*
2007/2008	432.8 *(115.2)*	24.5 *(105.3)*	408.4 *(125.1)*
2008/2009	526.9 *(119.7)*	52.4 *(95.3)*	474.5 *(144.2)*

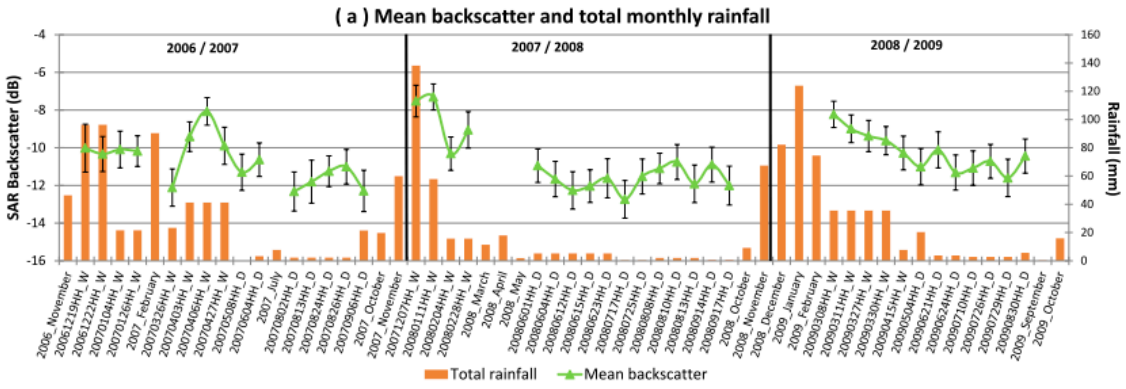

Figure 2. *Cont.*

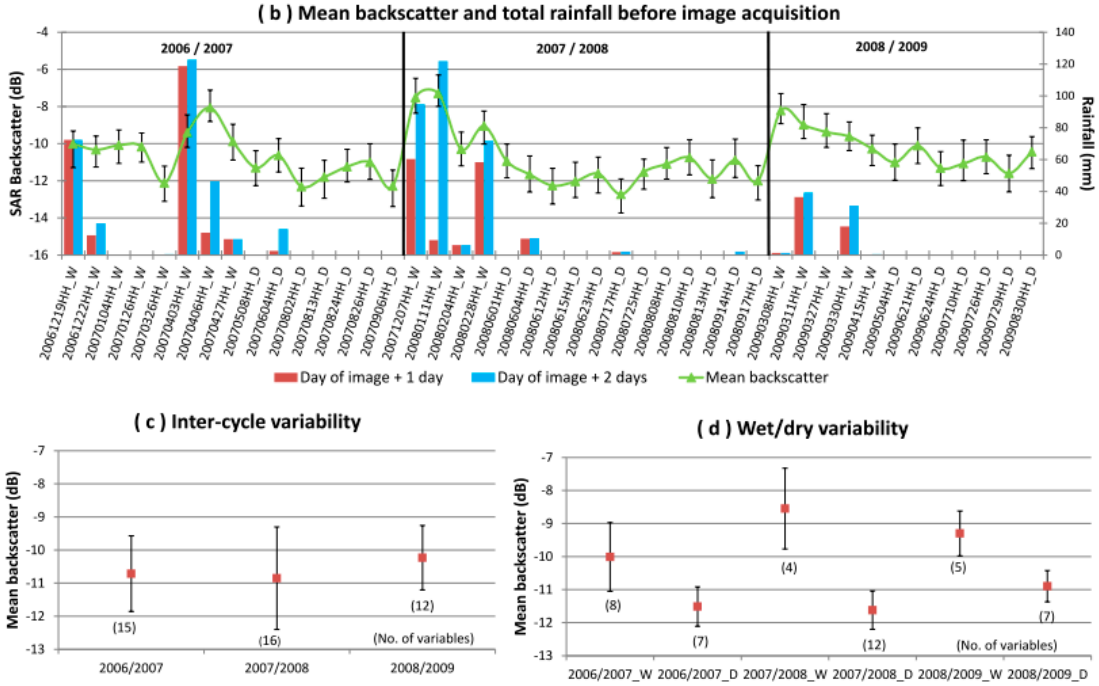

Figure 2. (**a**–**d**): Backscatter response to moisture in the landscape. The following is represented: (**a**) the mean backscatter per image and the total rainfall (i) per month and (ii) per month in which the image was acquired; (**b**) the mean backscatter and the total rainfall for the day of, plus one and two days prior to, image acquisition; (**c**) the inter-cycle mean backscatter values and associated variability (i.e., standard deviation); (**d**) and the mean backscatter values and associated variability between each wet and dry period. Months without images are labelled with the year and month accordingly (e.g., October 2006). Bracketed numbers represent the number of images in a series.

4.2. Effects of Temporal Filter, Model, and Metric

It has previously been established that the SAR backscatter is better correlated to woody structure under dry (leaf-off) conditions rather than wet (leaf-on) conditions in deciduous savannas [21]. As a result, the combination of 12 dry images from the 2007/2008 cycle (longest dry time series) was first used to test the effects of temporal filtering and investigate the differences in achievable accuracies between the two ML and RF models. Results for the above scenario are presented in Table 2. Since TCV is a unitless proxy for canopy volume, we compare the two sets of results using the relative RMSE (rRMSE) value.

The results in Table 2 show that in majority of the cases the TCV metric achieved marginally (i.e., <1% rRMSE) higher accuracies than the TCC metric for the tested scenarios. There are also clear improvements in the modelling performance as the temporal filtering window size is increased. With increasing temporal filter window size; (a) the SISA mean values remain in the region of 1, indicating the preservation of the original mean image values; (b) the SISA Stdev values increase, indicating improved speckle suppression. The random forest model produced improved accuracies over the multi-linear model, especially at increasing filter window sizes. The maximum TCC improvement for the 11 × 11 pixel filter was ~2.4% rRMSE, while for TCV it was 3.2% rRMSE.

Table 2. The TCC and TCV results for the 2007/2008 Dry scenario, using different temporal filtering treatments and different models. The filter's ability to preserve the image mean (i.e., $SISA_{mean}$) and suppress speckle (i.e., $SISA_{Stdev}$) are also represented.

TCC										
	Speckle Suppression		**Multi-Linear Regression**				**Random Forest**			
Scenario	**$SISA_{mean}$**	**$SISA_{Stdev}$**	**R^2 (CI)**	**RMSE (CI)**	**rRMSE (CI)**	**Bias**	**R^2 (CI)**	**RMSE (CI)**	**rRMSE (CI)**	**Bias**
Unfiltered	-	-	0.6 (0.002)	10.35 (0.043)	43.09 (0.002)	0.00	0.6 (0.003)	10.36 (0.044)	43.15 (0.002)	−0.05
3 × 3 Filter	1	0.2	0.62 (0.003)	10.05 (0.034)	41.56 (0.002)	−0.01	0.64 (0.003)	9.86 (0.034)	40.75 (0.002)	−0.02
7 × 7 Filter	0.99	0.27	0.66 (0.002)	9.52 (0.028)	39.63 (0.001)	0.09	0.69 (0.003)	9 (0.046)	37.47 (0.002)	0.05
11 × 11 Filter	0.99	0.28	0.68 (0.003)	9.24 (0.03)	38.53 (0.001)	−0.01	0.72 (0.002)	8.66 (0.032)	36.1 (0.002)	−0.12
TCV										
	Speckle Suppression		**Multi-Linear Regression**				**Random Forest**			
Scenario	**$SISA_{mean}$**	**$SISA_{Stdev}$**	**R^2 (CI)**	**RMSE (CI)**	**rRMSE (CI)**	**Bias**	**R^2 (CI)**	**RMSE (CI)**	**rRMSE (CI)**	**Bias**
Unfiltered	-	-	0.64 (0.004)	22,806.7 (72.9)	42.57 (0.002)	−29.88	0.64 (0.004)	22,578.4 (88.1)	42.14 (0.002)	−17.7
3 × 3 Filter	1	0.2	0.66 (0.003)	21,982 (85.5)	40.62 (0.002)	50.73	0.69 (0.003)	21,210.6 (89.9)	39.19 (0.002)	−120.3
7 × 7 Filter	0.99	0.27	0.69 (0.003)	20,981.9 (88.8)	39.38 (0.002)	−159.01	0.74 (0.003)	19,449.6 (108.8)	36.5 (0.003)	−288.9
11 × 11 Filter	0.99	0.28	0.71 (0.003)	20,396.6 (81.5)	38.42 (0.001)	70.00	0.76 (0.003)	18,710.1 (103.4)	35.24 (0.002)	−97.8

* R^2 = coefficient of determination; RMSE = Root mean square error (TCC unit is %, TCV is unit less); rRMSE = Relative RMSE (%), Bias = estimation bias (TCC unit is %, TCV is unit less), CI = 95% confidence interval (± around the mean).

The observed versus predicted scatter plots are presented in Figure 3a–d for the above mentioned 2007/2008 Dry (11 × 11 pixel filter) scenario. While the estimation bias is low for all scenarios, we see in comparison to the 1:1 line, the model predictions for both the TCC and TCV metrics are clearly overestimated at the lower end of the range, and underestimated at the top end of the range.

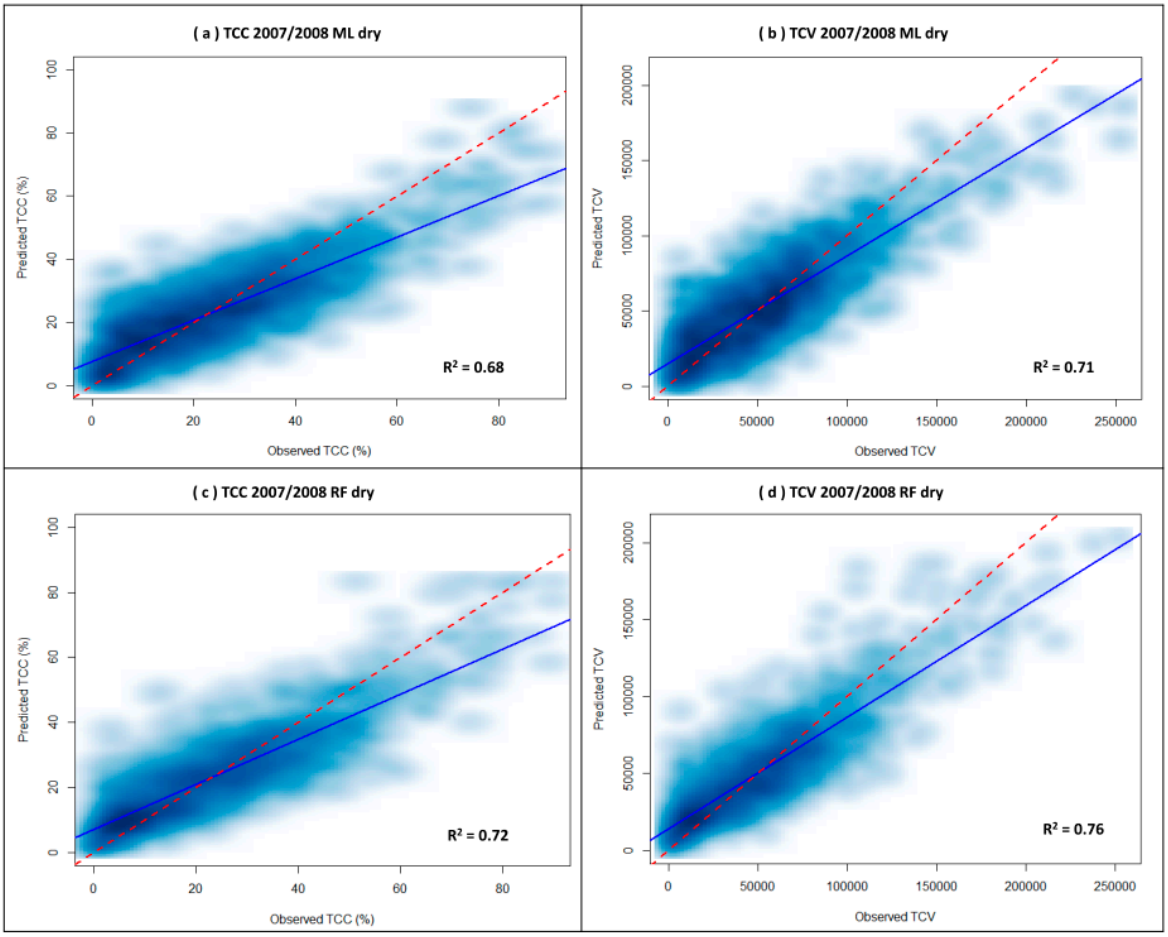

Figure 3. (**a**–**d**): Observed versus predicted scatterplots for the multi-linear regression (ML) and random forest (RF) 2007/2008 Dry scenario, both for the (**a**,**c**) TCC and (**b**,**d**) TCV metrics. The red dashed line represents the 1:1 line.

4.3. Wet and Dry Period Combinations

In accordance with the previous results, the remainder of the analyses focus only on the RF model and the 11 × 11 pixel temporally filtered images. The scenarios were split into phenological cycles and into wet and dry periods in order to investigate the strength of the relationships throughout these seasonal shifts (Table 3).

Two of the three dry periods (2006/2007 and 2008/2009) had a similar number of images and showed comparable results, for both TCC and TCV. The third dry period (2007/2008) produced the highest accuracies, which might be due to, (i) six more dry images in this scenario; (ii) the 2007/2008 dry period received the least amount of rainfall; and (iii) the LiDAR data were acquired in the same year. Unlike the dry periods, the wet period results showed more variation, for each metric and between annual cycles. The high accuracies produced by the 2006/2007 wet period were unexpected, as they are higher than the dry image combination of the same year and similar to the dry scenarios of the two other years (2007/2008 and 2008/2009). This result was despite rainfall records (Figure 2b) showing that five of the eight images received rainfall just prior to image acquisition, but may also have been supported by a higher number of images (eight compared to four or five in the other annual

cycles). The poorest wet period results for both metrics (i.e., 2008/2009) coincide with the cycle, and wet period, that received the most rainfall (Table 1). The 2008/2009 wet scenario, with five images, should be most comparable to the 2007/2008 wet scenario with four images, but the 2008/2009 wet season received 35% more rain which may explain the significant difference in performance. For all annual cycles, the addition of the wet period images to the dry period images appears to add sufficient additional information for the model to produce improved accuracies.

Table 3. Filtered random forest rRMSE results for different combinations of dry (D) and wet (W) period imagery within each phenological cycle, and for both the TCC and TCV LiDAR metrics.

	TCC				TCV				
	R^2 (CI)	RMSE (CI)	rRMSE (CI)	Bias	R^2 (CI)	RMSE (CI)	rRMSE (CI)	Bias	Variables
2006/2007_W	0.7 (0.004)	8.92 (0.059)	36.8 (0.003)	−0.06	0.74 (0.004)	19,481.3 (102.9)	36.41 (0.002)	−429.9	8
2006/2007_D	0.67 (0.004)	9.32 (0.045)	38.72 (0.003)	0.00	0.7 (0.004)	20,813 (112)	38.32 (0.002)	−10.8	7
2006/2007_WD	0.76 (0.004)	8.03 (0.052)	33.32 (0.003)	−0.06	0.79 (0.003)	17,578.9 (92.7)	32.64 (0.002)	−262.6	15
2007/2008_W	0.63 (0.004)	9.99 (0.059)	41.64 (0.003)	−0.03	0.67 (0.005)	21,613.8 (152.7)	40.37 (0.003)	−168.9	4
2007/2008_D	0.72 (0.002)	8.66 (0.032)	36.1 (0.002)	−0.12	0.76 (0.003)	18,710.1 (103.4)	35.24 (0.002)	−97.8	12
2007/2008_WD	0.75 (0.003)	8.21 (0.047)	33.79 (0.002)	−0.09	0.79 (0.003)	17,533.8 (104.2)	33.15 (0.002)	−229.7	16
2008/2009_W	0.51 (0.005)	11.5 (0.056)	47.91 (0.003)	−0.13	0.57 (0.007)	24,885.5 (178)	46.19 (0.003)	−443.4	5
2008/2009_D	0.67 (0.004)	9.29 (0.044)	38.4 (0.002)	−0.02	0.72 (0.004)	20,110.7 (127.6)	37.61 (0.002)	−26.8	7
2008/2009_WD	0.7 (0.003)	8.96 (0.037)	37.35 (0.002)	0.01	0.73 (0.004)	19,566.9 (127.8)	36.37 (0.002)	−143	12
All Dry Images	0.75 (0.004)	8.22 (0.045)	34.1 (0.002)	0.01	0.78 (0.003)	17,942.7 (112.2)	33.96 (0.002)	−22.5	26
All Images	0.77 (0.003)	7.78 (0.053)	31.77 (0.002)	−0.19	0.8 (0.003)	16,846.5 (95.3)	31.31 (0.002)	−267.4	43

* R^2 = coefficient of determination; RMSE = Root mean square error (TCC unit is %, TCV is unitless); rRMSE = Relative RMSE (%), Bias = estimation bias (TCC unit is %, TCV is unit less), CI = 95% confidence interval (±around the mean).

Again, the differences in rRMSE between TCC and TCV were marginal, but TCV does maintain a consistently lower rRMSE throughout. If we combine all 26 dry images, and compare to the best single dry period result (i.e., 2007/2008_D), the rRMSE values only show an improvement of between 2% and 1.3% for TCC and TCV respectively, but using 14 additional images. The combination of wet and dry images for each of the 2006/2007 and 2007/2008 cycles produced higher accuracies, and using less imagery than all the dry images combined. Combining all wet and dry images (43), results in a rRMSE improvement over the 26 dry images of ca. 2.3% for TCC and ca. 2.6% for TCV. This implies limited new information is available to the model after a certain number of images are added.

4.4. Image Sequences

The following analysis added images sequentially to the model(s) in order to assess model improvement over the course of each phenological cycle, and attempt to determine a balance between number of images required and model accuracy. The first scenario involved investigating how accuracies change over the course of each phenological cycle, beginning with the higher accuracy dry

images and then adding the wet images. The next scenario, investigated whether using multi-cycle dry images only would produce higher accuracies than single-cycle dry, or dry and wet, image combinations. The final scenario investigated how model performance might be affected when all the wet and dry (in date order) images were added across the three phenological cycles. The results of the first scenario (i.e., individual cycles) are presented in Figure 4a–f), were we found a similar pattern of improvement in the rRMSE results for each cycle, and for both metrics. The two cycles 2007/2008 and 2008/2009 produced the most accuracy gain using between six and nine (dry) images respectively (Figure 4c–f). As described in sections above, the wetter 2008/2009 cycle produced results that were lower than the other cycles, and with a more tempered relative improvement as each image is added to the sequence (Figure 4e–f). The 2006/2007 cycle exhibits a slightly more linear pattern, with a less obvious plateau in the performance than the other cycles (Figure 4a,b).

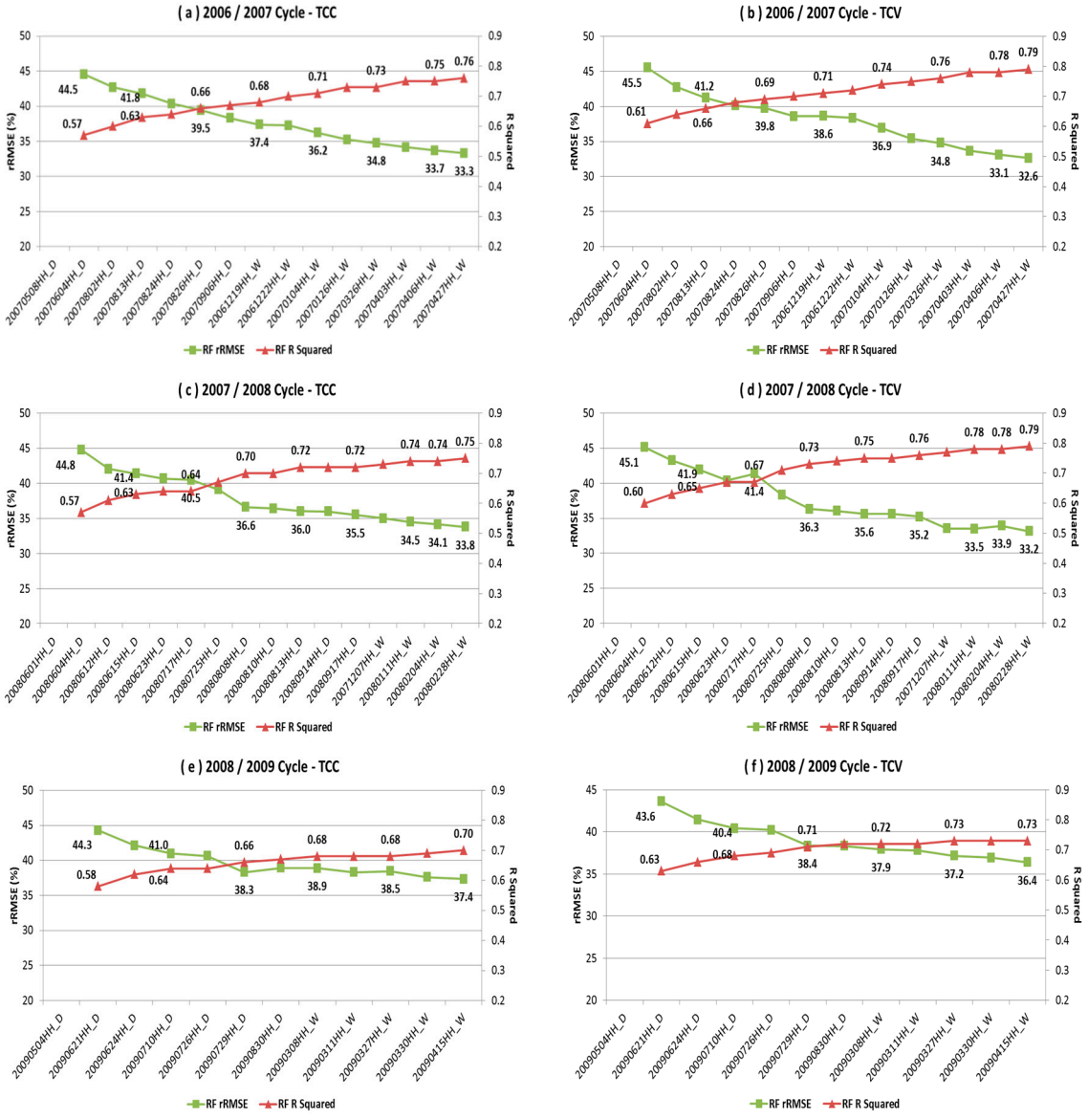

Figure 4. (**a**–**f**): Results from the sequential addition of the individual dry and wet images, per phenological cycle, to the modelling process, for both TCC and TCV metrics. The first two images of each scenario are used as the starting combination.

When adding only dry images in sequence over multiple cycles the following results were achieved (Figure 5a,b). For both TCC and TCV, using three cycles of dry images elicited an initial prompt improvement in the rRMSE results, before minimal gain in performance (i.e., plateau) is reached when 8 to 12 images have been added. Comparing an rRMSE result at this plateau to the final (rRMSE) result only equates to an improvement of ~2% for both metrics, but at a cost of ~16 additional images. If we remove the images of the first cycle, and begin with the cycle that coincides with the year of LiDAR acquisition and the least rainfall (2007/2008), then we see very similar trends and only marginally different final results, despite using seven fewer images. Using only two cycles a point of minimal gain appears to be reached after 8 to 10 images were added, for both metrics.

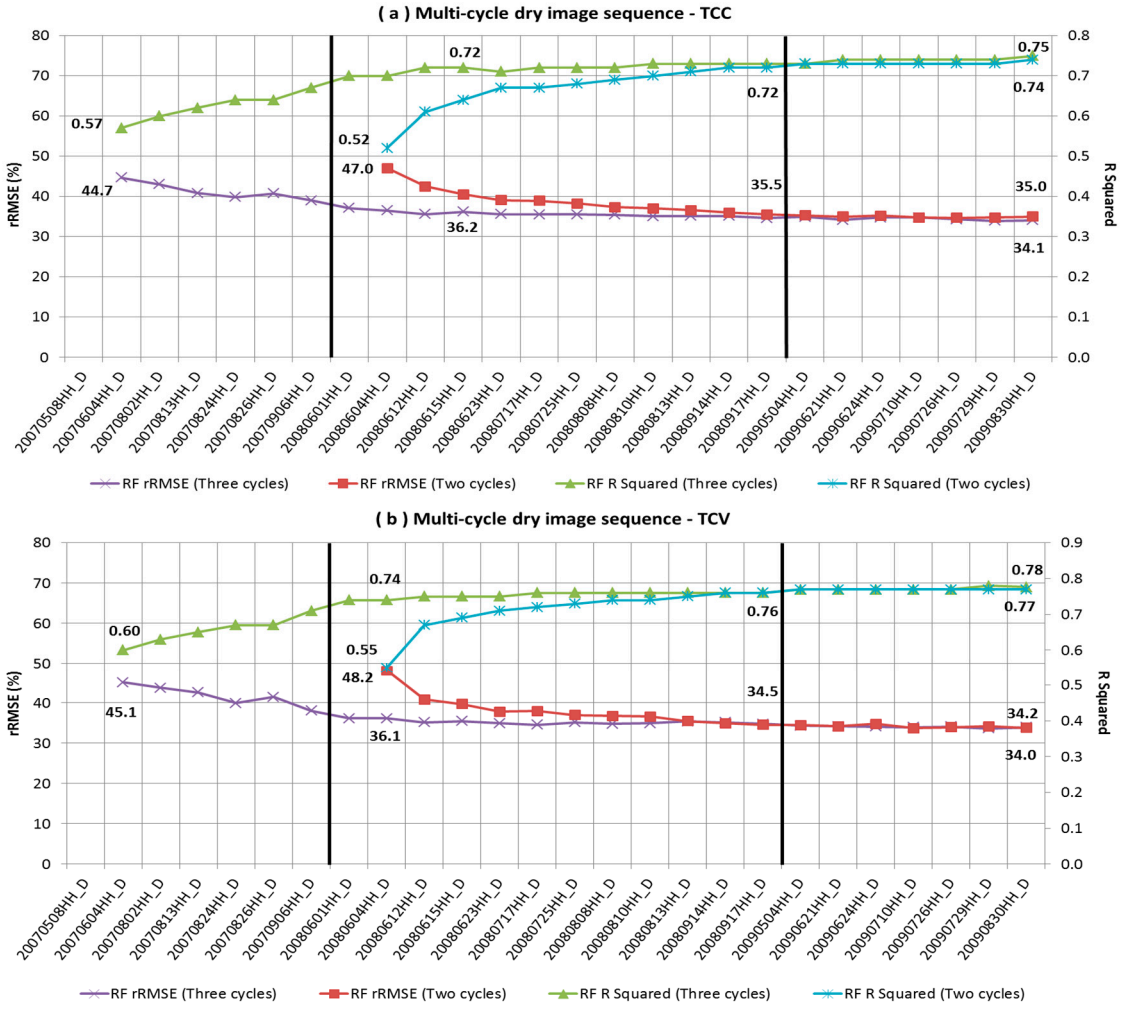

Figure 5. (**a**,**b**): Results from the sequential addition to the model of dry images from: (i) all three cycles of images; (ii) only two cycles of images, for both TCC (**a**) and TCV (**b**) metrics The first two images of each scenario are used as the starting combination. Data labels are provided for the first result, the approximate plateau, as well as the final result in the sequence.

Using all the wet and dry images (43 images) from the three cycles produces similar trends as above, and naturally produces the highest accuracies of the study, for both TCC (RF model: R^2 = 0.77, RMSE = 7.78%, rRMSE = 31.77%) and TCV (RF model: R^2 = 0.8, RMSE = 16846.54, rRMSE = 31.31%) (Figure 6a,b). The scenario of using the images in date order simulates an operational scenario in which the images are used as they become available. For both the TCC and TCV metrics there is the same rapid initial improvement in the model accuracies, despite beginning the sequence with wet images. The first cycle (2006/2007), contains images that elicited a sustained improvement in the results, hence a

plateau in performance is reached towards the later stages of that cycle (i.e., 12–14 images) when using the three cycle sequence, for both metrics. Using only two cycles of images, the initial improvement in results is more rapid before it tapers off, and then appears to reach a plateau in the middle of the 2007/2008 cycle (i.e., 7–8 images), for both metrics. There were no significant improvements in the results as the sequence of images transitions across the rest of the wet and dry periods making up the remaining cycles. In summary, whether one uses dry images only, or wet and dry images, there appears to be no significant advantage to processing more than one phenological cycle worth of images.

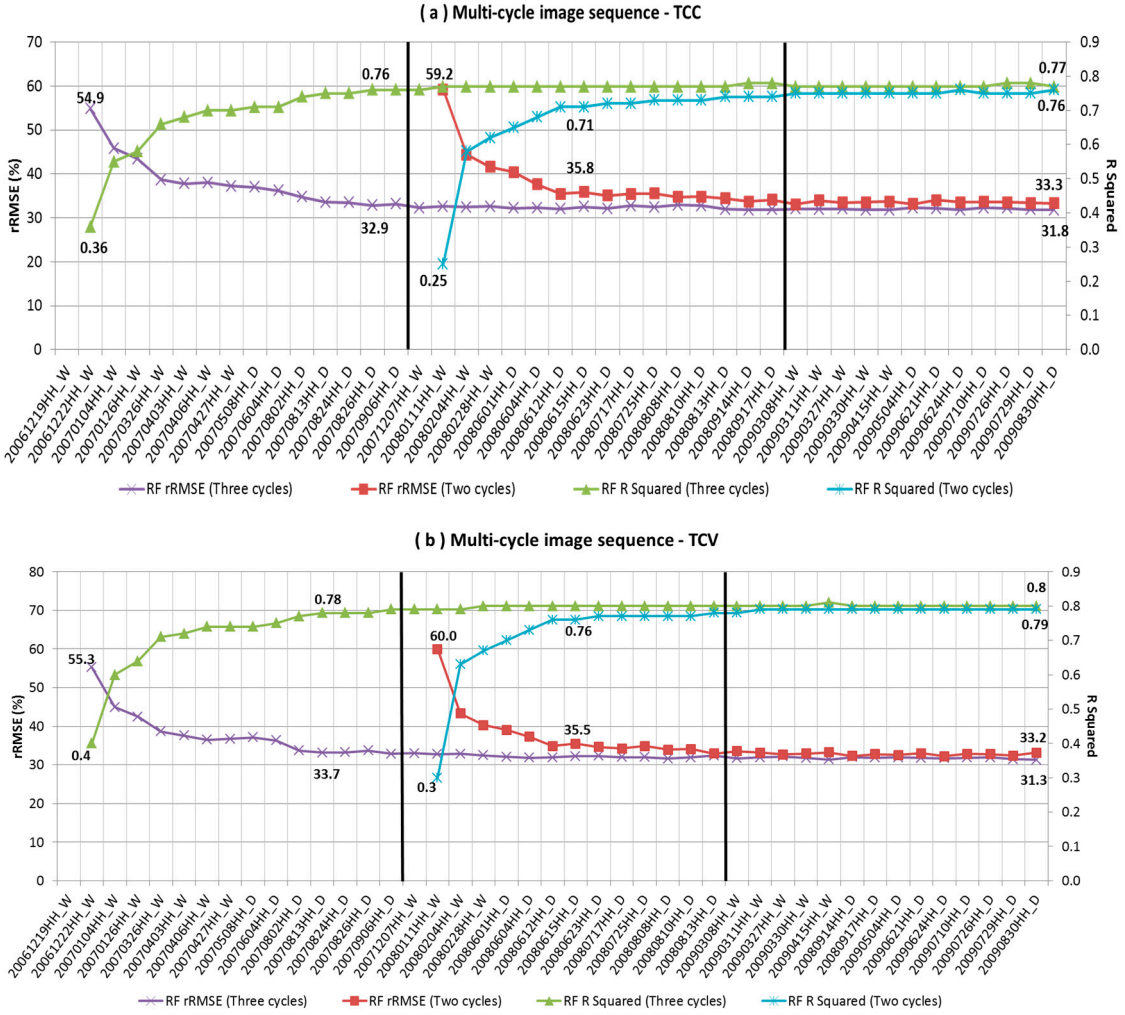

Figure 6. (**a**,**b**): Results from the sequential addition to the model of date ordered wet and dry images from: (i) all three cycles of images; (ii) only two cycles of images, for both TCC (**a**) and TCV (**b**) metrics. The first two images of each scenario are used as the starting combination. Data labels are provided for the first result, the approximate plateau, as well as the final result in the sequence.

5. Discussion

The analysis presented above has explored the relationship between a time series of C-band SAR and woody structural metrics (TCC and TCV) for a deciduous savanna environment, and the results are discussed here. Firstly, the application of a temporal filter to the C-band time series acted to reduce the amount of variance (i.e., speckle) in the images, and in doing so consistently improved upon unfiltered prediction accuracies using various window sizes. The savanna is a spatially variable environment, and vegetation structure, phenology, and patterns of vegetation distribution are largely

influenced by geology and inconstant amounts of moisture within the landscape [2,30,41]. The geology and moisture vary at differing scales, such as across catenal positions, as well as at larger scales such as East to West and North to South [30]. The subsequent variability in vegetation distribution and structure within the landscape, which is captured in the LiDAR, was evidently still retained in the SAR images despite the spatial detail of the SAR images being degraded by the different temporal filter window sizes used. This shows that together with the large (i.e., 150 m × 150 m) sampling window, the increase in the size of the filter window acted to continuously smooth the SAR data (temporally and spatially) of adverse speckle and co-registration effects (i.e., noise), to the point where the SAR data became better correlated with the aggregated LiDAR data and overall modelling accuracies improved. An added benefit of the temporal filter is that it can be used to filter images from different sensors. Meaning that historical ASAR data could potentially be used to temporally filter data from new generation of sensors, such as Sentinel1 [32], which would benefit the continuity between the systematically collected (C-band) SAR sensors (i.e., Envisat ASAR and Sentinel-1).

The relationship between the C-band SAR backscatter and LiDAR metrics was well described by the linear regression model, however the non-linear random forest model ultimately produced the higher accuracies of the two models. The random forest model has been shown to be a robust model that is capable of capturing the complexity non-linear relationships, and is seldom affected by problems of overfitting [42,43]. The scatterplot of the validation for the model shows underestimation for high cover areas and overestimation for low cover areas (Figure 3). The underestimation in high cover areas can be explained by the C-band signals' limited ability in penetrating a dense canopy, and the LiDAR data included a limited amount of very dense vegetation; hence the top end of the TCC range is under-represented. At the lower end, limitations of the LiDAR in detecting low vegetation (e.g., <1.5 m tall) [44] would contribute to the overestimation, as would the interference and variability of soil texture and roughness, and grass biomass in these low woody cover areas.

Both TCC and TCV showed high levels of agreement with the temporally filtered ASAR data. Co-polarized (HH) C-band backscatter consists of volume scattering from leaves, twigs, and smaller branches in the upper canopy, but is generally regarded as being less sensitive than the HV polarization is to volume scattering effects [17]. Given the particular physiognomy of the savanna vegetation in this case, i.e., short, coppiced, and open canopy, there appear to be sufficient volume scatterers and sensitivity from the HH polarization to have produced the accuracies reported above. In agreement with other studies conducted in the region [16,18], the TCV metric in particular achieved consistently higher accuracies compared to TCC. This could be explained by the fact that TCV is a three-dimensional metric representing the volume of vegetation within the vertical profile [21,35], the volume being represented is of an open canopy environment that enables the SAR signal to reach beyond the upper portions of the canopy thereby interacting with the similar elements of the vegetation vertical profile from which the LiDAR metric was derived.

The influence of moisture, via rainfall, on the backscatter response was investigated and it showed that the SAR backscatter responded to precipitation events with high backscatter response and variability, whereas dry periods resulted in a lower and less variable mean backscatter response. The influence of moisture on the SAR signal appeared to play out at two different scales, namely (i) at the image scale where backscatter appeared to increase in response to rainfall amounts received prior to the image being captured; and (ii) at the phenological cycle scale where we see wetter cycles (i.e., 2008/2009) exhibit higher mean backscatter values compared to drier cycles. As was expected from similar studies in the savanna [21], the wet image combinations had an overall lower predictive accuracy than dry image combinations. However, it is difficult to conclude on the role of wet images in this study as the three cycles produced quite varied results. We would expect comparable results for the two scenarios with similar numbers of wet images (i.e., 2007/2008 with four images and 2008/2009 with five images), but this was not the case as the 2008/2009 wet scenario produced the worst result of the study (Table 3). This (2008/2009) wet scenario did not experience significant amounts of rainfall shortly before image acquisition, unlike the other two scenarios, but did experience

the highest total rainfall over the course of the wet period. It could be speculated that the short term effects of moisture on the SAR backscatter had less of an impact on the results than the potential increases in foliage cover within the landscape due to long(er) term accumulated moisture. The fact that two out of three wet scenarios still produced reasonable results (i.e., $R^2 > 0.6$), may affirm the findings of [14] that open canopy environments negate much of the expected increase in attenuation and depolarization of backscatter that is usually associated with increases of canopy foliage during growing periods. The wetter 2008/2009 cycle being the exception here. In summary, wet images had generally a positive influence on model accuracy when added to dry period images, except in instances where the leaf-on period and/or the phenological cycle in question was exceptionally wet. Hence, a decision on whether to include wet images in an analysis, could weigh up the following: (i) the number of dry images available versus the cost of processing the wet images; and (ii) particularly high volumes of precipitation received over the course of the wet period.

The performance of the dry images is consistent with other literature, which indicates that dry, or leaf-off, conditions are the best for vegetation parameter estimation using SAR in savanna environments [10,15,16,18]. With majority of the tree species in the region being deciduous the dry period produces a 'leaf-off' situation that results in increased transparency within the canopy, thereby allowing the SAR signal to penetrate further into the canopy. The SAR signal would therefore interact with more woody elements, rather than the canopy foliage of the vegetation [37,45]. The dry period also brings about a decrease in the moisture of the soil and grass [21,46].

The accuracies achieved are similar in magnitude to other studies in the region which used higher resolution SAR imagery (e.g., 12.5–25 m), with more appropriate polarizations (e.g., HV), and more capable frequencies (e.g., L-band) [15,16,18]. While studies such as [15,16] point to the HV polarization and the L-band wavelength as being particularly sensitive to vegetation parameters, the results from the present study show that co-polarized (i.e., HH) C-band data are a viable alternative in this savanna environment. For example, a series of only seven dry period images (e.g., 2007/2008), could produce accuracies for TCV of $R^2 = 0.72$ and rRMSE = 37.61%, which are very close to the (TCV) accuracies achieved by [21] using multi-season quad-pol RADARSAT-2 data ($R^2 = 0.71$, rRMSE = 36.85%). The TCC results from the same (2007/2008) series of images ($R^2 = 0.67$, RMSE = 9.29%) are also comparable to the single dual-pol dry image L-band accuracies achieved by [15] ($R^2 = 0.66$, RMSE = 8.45%). There does, however, appear to be a limit to the amount of useful information that a high number of images can add to the model(s). The point at which most of the variability had been described differs amongst the scenarios, but was generally between 6 and 10 images, and which frequently produced accuracies that were the equivalent of 10% RMSE or 41% rRMSE. The results bode well for making use of Sentinel-1 C-band data in a similar fashion, as it has an improved revisit time, higher spatial resolution (i.e., ~20 m), as well as the cross-polarized VH data available.

It is possible to obtain high accuracies (i.e. $R^2 > 0.75$, rRMSE ~30%) using all 43 images, however, it would be prudent to weigh up the time and effort required to process these against the diminishing accuracy gained. In this savanna environment, a single phenological cycle, or a single dry period produced accuracies that were only marginally lower than the highest accuracies achieved. An ideal scenario, such as the 2007/2008 dry scenario that had the lowest rainfall, the highest number of dry period images (i.e., 12), and which coincided with the year of LiDAR acquisition, achieved results that were only 2% to 3% (rRMSE) lower than scenarios that used double the number of dry images (i.e., all 26 dry images) (Table 3). Outside of those ideal combinations, the remaining two cycles still achieved results that were only 4% to 5 % (rRMSE) lower than when using all the dry images, even in the instance of the wettest (2008/2009) cycle. Being able to achieve such results using only one phenological cycle of images does not only reduce the cost and amount of processing required, but will also mean that change detection studies are possible without the complication of using imagery that spans phenological cycles. This demonstrates the potential of monitoring woody vegetation

structure with C-band time series, and provides a guide to the initial temporal range, and number of images, that need to be acquired and processed to achieve useful levels of accuracy.

6. Conclusions

We investigated the strength of the relationships between a time series of C-band, ASAR-WS SAR imagery, and two LiDAR-derived woody structural metrics—total canopy cover (TCC) and total canopy volume (TCV)—within a Southern African savanna environment. The accuracies presented here, for both metrics, were comparable to studies that made use of commercial high resolution L-band SAR data [15,20]. High prediction accuracies were achieved despite the SAR wavelength (i.e., C-band), the spatial resolution (i.e., 75 m), and the single polarization (i.e., HH) being sub-optimal SAR data for woody vegetation structure estimation. The hyper-temporal nature of the dataset, the application of the temporal filter, and the physiognomy of the vegetation contributed to off-set these potential disadvantages, by increasing vegetation related backscatter, reducing the variance due to noise, and increasing volume related backscatter through increased canopy penetration. Dry images produced the best results, as expected, while the performance and contribution of the wet images was varied and appeared to be linked with longer term moisture accumulation, and associated foliage cover, rather than individual rainfall incidents. However, in two out of three cycles, the wet images did contribute towards the results of a single phenological cycle being equivalent to three cycles of dry images. So, depending on the environmental conditions at the time, the analysis shows that very reasonable results can be achieved using the wet and dry images of a single phenological cycle, consisting of between 6 to 10 images, with the potential to achieve higher accuracies should there be the capacity to process additional images.

The study is unique in its application of hyper-temporal SAR datasets for woody parameters estimation in a deciduous savanna environment, and the findings will inform: (a) work that seeks to use archive data to create regional baseline maps; and (b) future work seeking to use new generation C-band SAR sensors (e.g., ESA's Sentinel-1) to create more recent woody structure map products, which can then be compared to baseline maps for change investigations. With both the ASAR archive (2002–2011) and Sentinel-1 C-band (2014-present) data being freely available, there now exists a significant amount of data which can be exploited in order to improve the historically poor monitoring and reporting efforts for woody resources in Southern Africa, both at regional and national scales. The results of this paper not only provide some level of confidence in the capability of freely available C-band data, but also point to how best large amounts of similarly polarized data can be efficiently used. The contribution of (historical) precision calibration LiDAR data in this study cannot be understated, and the availability of additional LiDAR data presents an opportunity to expand this research to different regions, using new generation SAR sensors. Given the costs involved in acquiring LiDAR data, innovative partnerships and collaborations between research organizations, government departments, and the private sector are being explored in order to address this.

Acknowledgments: The authors acknowledge the Council for Scientific and Industrial Research (CSIR), the German Federal Ministry of Education and Research (BMBF) funded SASSCAL project (Work package 3, Task 205), and the European Union's seventh framework program (grant No. 282621, AGRICAB) for funding this study. The Carnegie Airborne Observatory is made possible by the Avatar Alliance Foundation, Margaret A. Cargill Foundation, John D. and Catherine T. MacArthur Foundation, Grantham Foundation for the Protection of the Environment, W.M. Keck Foundation, Gordon and Betty Moore Foundation, Mary Anne Nyburg Baker and G. Leonard Baker Jr., and William R. Hearst III. The application of the CAO data in South Africa is made possible by the Andrew Mellon Foundation, Grantham Foundation for the Protection of the Environment, and the endowment of the Carnegie Institution for Science. The LiDAR data was processed by T. Kennedy-Bowdoin, D. Knapp, J. Jacobson, and R. Emerson at the Carnegie Institute for Science. The South African Weather Service (SAWS) and South African National Parks (SANParks) scientific services are also both acknowledged for supplying rainfall data.

Author Contributions: Russell Main, Renaud Mathieu, Konrad Wessels, and Waldo Kleynhans conceived and designed the experiment. Waldo Kleynhans performed the SAR processing by GAMMA Software. Laven Naidoo contributed to SAR processing, statistical modelling, and the interpretation of results. Greg Asner, through the CAO campaign and acknowledged partners, provided funding for the LiDAR acquisition and LiDAR processing, as well as interpretation and review of the results. Renaud Mathieu and Konrad Wessels also provided interpretation and review of data and manuscripts. Russell Main analyzed the outcomes, interpreted data, and wrote the paper.

Conflicts of Interest: The authors declare no conflict of interest.

References

1. Scholes, R.J.; Archer, S.R. Tree-grass interactions in savannas. *Ecology* **2013**, *28*, 517–544.
2. Sankaran, M.; Hanan, N.P.; Scholes, R.J.; Ratnam, J.; Augustine, D.J.; Cade, B.S.; Gignoux, J.; Higgins, S.I.; Le Roux, X.; Ludwig, F.; et al. Determinants of woody cover in African savannas. *Nature* **2005**, *438*, 846–849. [CrossRef] [PubMed]
3. Twine, W.; Moshe, D.; Netshiluvhi, T.; Siphungu, V. Consumption and direct-use values of savanna bio-resources used by rural households in Mametja, a semiarid area of Limpopo province, South Africa. *S. Afr. J. Sci.* **2003**, *99*, 467–473.
4. Shackleton, C.M.; Shackleton, S.E. The importance of non-timber forest products in rural livelihood security and as safety nets: A review of evidence from South Africa. *S. Afr. J. Sci.* **2004**, *100*, 658–664.
5. Valentini, R.; Arneth, A.; Bombelli, A.; Castaldi, S.; Cazzolla Gatti, R.; Chevallier, F.; Ciais, P.; Grieco, E.; Hartmann, J.; Henry, M.; et al. A full greenhouse gases budget of Africa: Synthesis, uncertainties, and vulnerabilities. *Biogeosciences* **2014**, *11*, 381–407. [CrossRef]
6. Matsika, R.; Erasmus, B.F.N.; Twine, W.C. A tale of two villages: Assessing the dynamics of fuelwood supply in communal landscapes in South Africa. *Environ. Conserv.* **2012**, *40*, 1–13. [CrossRef]
7. Wigley, B.J.; Bond, W.J.; Hoffman, M.T. Bush encroachment under three contrasting land-use practices in a mesic South African savanna. *Afr. J. Ecol.* **2009**, *47*, 62–70. [CrossRef]
8. Knapp, A.K.; Briggs, J.M.; Collins, S.L.; Archer, S.R.; Bret-harte, M.S.; Ewers, B.E.; Peters, D.P.; Young, D.R.; Shaver, G.R.; Pendall, E.; et al. Shrub encroachment in North American grasslands: Shifts in growth form dominance rapidly alters control of ecosystem carbon inputs. *Glob. Chang. Biol.* **2008**, *14*, 615–623. [CrossRef]
9. Santos, J.R.; Lacruz, M.S.P.; Araujo, L.S.; Keil, M. Savanna and tropical rainforest biomass estimation and spatialization using JERS-1 data. *Int. J. Remote Sens.* **2002**, *23*, 1217–1229. [CrossRef]
10. Mitchard, E.T.A.; Saatchi, S.S.; Lewis, S.; Feldpausch, T.R.; Woodhouse, I.H.; Sonké, B.; Rowland, C.; Meir, P. Measuring biomass changes due to woody encroachment and deforestation/degradation in a forest–savanna boundary region of central Africa using multi-temporal L-band radar backscatter. *Remote Sens. Environ.* **2011**, *115*, 2861–2873. [CrossRef]
11. Dobson, M.C.; Ulaby, F.T.; Le Toan, T.; Beaudoin, A.; Kasischke, E.S.; Christensen, N. Dependance of radar backscatter on coniferous forest biomass. *IEEE Trans. Geosci. Remote Sens.* **1992**, *30*, 412–415. [CrossRef]
12. Le Toan, T.; Beaudoin, A.; Riom, J.; Guyon, D. Relating forest biomass to SAR data. *IEEE Trans. Geosci. Remote Sens.* **1992**, *30*, 403–411. [CrossRef]
13. Mitchard, E.T.A.; Saatchi, S.S.; White, L.; Abernethy, K.; Jeffery, K.; Lewis, S.L.; Collins, M.; Lefsky, M.A.; Leal, M.E.; Woodhouse, I.H.; et al. Mapping tropical forest biomass with radar and spaceborne LiDAR in Lopé National Park, Gabon: Overcoming problems of high biomass and persistent cloud. *Biogeosciences* **2012**, *9*, 179–191. [CrossRef]
14. Lucas, R.M.; Cronin, N.; Lee, A.; Moghaddam, M.; Witte, C.; Tickle, P. Empirical relationships between AIRSAR backscatter and LiDAR-derived forest biomass, Queensland, Australia. *Remote Sens. Environ.* **2006**, *100*, 407–425. [CrossRef]
15. Urbazaev, M.; Thiel, C.; Mathieu, R.; Naidoo, L.; Levick, S.R.; Smit, I.P.J.; Asner, G.P.; Schmullius, C. Assessment of the mapping of fractional woody cover in southern African savannas using multi-temporal and polarimetric ALOS PALSAR L-band images. *Remote Sens. Environ.* **2015**, *166*, 138–153. [CrossRef]
16. Ningthoujam, R.; Balzter, H.; Tansey, K.; Morrison, K.; Johnson, S.; Gerard, F.; George, C.; Malhi, Y.; Burbidge, G.; Doody, S.; et al. Airborne S-band SAR for forest biophysical retrieval in temperate mixed forests of the UK. *Remote Sens.* **2016**, *8*, 609. [CrossRef]

17. Lucas, R.M.; Moghaddam, M.; Cronin, N. Microwave scattering from mixed-species forests, Queensland, Australia. *IEEE Trans. Geosci. Remote Sens.* **2004**, *42*, 2142–2159. [CrossRef]
18. Askne, J.; Santoro, M. Multitemporal repeat pass SAR interferometry of boreal forests. *IEEE Trans. Geosci. Remote Sens.* **2005**, *43*, 1219–1228. [CrossRef]
19. Pulliainen, J.T.; Mikkela, P.J.; Hallikainen, M.T.; Ikonen, J.P. Seasonal dynamics of C-band backscatter of boreal forests with applications to biomass and soil moisture estimation. *IEEE Trans. Geosci. Remote Sens.* **1996**, *34*, 758–770. [CrossRef]
20. Naidoo, L.; Mathieu, R.; Main, R.; Kleynhans, W.; Wessels, K.; Asner, G.P.; Leblon, B. Savannah woody structure modelling and mapping using multi-frequency (X-, C- and L-band) Synthetic Aperture Radar data. *ISPRS J. Photogramm. Remote Sens.* **2015**, *105*, 234–250. [CrossRef]
21. Mathieu, R.; Naidoo, L.; Cho, M.A.; Leblon, B.; Main, R.; Wessels, K.; Asner, G.P.; Buckley, J.; van Aardt, J.A.N.; Erasmus, B.F.N.; et al. Toward structural assessment of semi-arid African savannahs and woodlands: The potential of multitemporal polarimetric RADARSAT-2 fine beam images. *Remote Sens. Environ.* **2013**, *138*, 1–17. [CrossRef]
22. Wang, D.; Lin, H.; Chen, J.; Zhang, Y.; Zeng, Q. Application of multi-temporal ENVISAT ASAR data to agricultural area mapping in the Pearl River Delta. *Int. J. Remote Sens.* **2010**, *31*, 1555–1572. [CrossRef]
23. Santoro, M.; Beer, C.; Cartus, O.; Schmullius, C.; Shvidenko, A.; McCallum, I.; Wegmüller, U.; Wiesmann, A. Retrieval of growing stock volume in boreal forest using hyper-temporal series of ENVISAT ASAR ScanSAR backscatter measurements. *Remote Sens. Environ.* **2011**, *115*, 490–507. [CrossRef]
24. Pulliainen, J.T.; Kurvonen, L.; Hallikainen, M.T. Multitemporal behavior of L- and C-band SAR observations of boreal forests. *IEEE Trans. Geosci. Remote Sens.* **1999**, *37*, 927–937. [CrossRef]
25. Askne, J.I.H.; Dammert, P.B.G.; Ulander, L.M.H.; Smith, G. C-band repeat-pass interferometric SAR observations of the forest. *IEEE Trans. Geosci. Remote Sens.* **1997**, *35*, 25–35. [CrossRef]
26. Santoro, M.; Schmullius, C.; Pathe, C.; Schwilk, J.; Beer, C.; Thurner, M.; Fransson, J.E.S.; Shvidenko, A.; Schepaschenko, D.; McCallum, I.; et al. Estimates of forest growing stock volume of the northern hemisphere from ENVISAT ASAR. In Proceedings of ESA Living Planet Symposium, Edinburgh, UK, 9–13 September 2013; pp. 714–722.
27. Townsend, P.A. Estimating forest structure in wetlands using multitemporal SAR. *Remote Sens. Environ.* **2002**, *79*, 288–304. [CrossRef]
28. Kumar, S.; Pandey, U.; Kushwaha, S.P.; Chatterjee, R.S.; Bijker, W. Aboveground biomass estimation of tropical forest from Envisat advanced synthetic aperture radar data using modeling approach. *J. Appl. Remote Sens.* **2012**, *6*, 1–18. [CrossRef]
29. Mucina, L.; Rutherford, M.C. (Eds.) *The Vegetation of South Africa, Lesotho and Swaziland*; South African National Biodiversity Institute: Pretoria, South Africa, 2006.
30. Venter, K.J.; Scholes, R.J.; Eckhardt, H.C. The abiotic template and its associated vegetation pattern. In *The Kruger Experience: Ecology and Management of Savanna Heterogeneity*; Du Toit, J., Biggs, H., Rogers, K.H., Eds.; London Island Press: London, UK, 2003; pp. 83–129.
31. GAMMA. Differential interferometry and geocoding software: DIFF&GEO. In *GAMMA: Geocoding and Image Registration Documentation: User's Guide*; GAMMA: Gümligen, Switzerland, 2008.
32. Quegan, S.; Yu, J.J. Filtering of multichannel SAR images. *IEEE Trans. Geosci. Remote Sens.* **2001**, *39*, 2373–2379. [CrossRef]
33. Sheng, Y.; Xia, Z. A comprehensive evaluation of filters for radar speckle suppression. *Int. Geosci. Remote Sens. Symp.* **1996**, *3*, 1559–1561.
34. Qiu, F.; Berglund, J.; Jensen, J.R.; Thakkar, P.; Ren, D. Speckle noise reduction in SAR imagery using a local adaptive median filter. *GISci. Remote Sens.* **2004**, *41*, 244–266. [CrossRef]
35. Asner, G.P.; Knapp, D.E.; Kennedy-Bowdoin, T.; Jones, M.O.; Martin, R.E.; Boardman, J.; Field, C.B. Carnegie Airborne Observatory: In-flight fusion of hyperspectral imaging and waveform light detection and ranging for three-dimensional studies of ecosystems. *J. Appl. Remote Sens.* **2007**, *1*, 1–21. [CrossRef]
36. Wessels, K.J.; Mathieu, R.; Erasmus, B.F.N.; Asner, G.P.; Smit, I.P.J.; van Aardt, J.A.N.; Main, R.; Fisher, J.; Marais, W.; Kennedy-Bowdoin, T.; et al. Impact of communal land use and conservation on woody vegetation structure in the Lowveld savannas of South Africa. *For. Ecol. Manag.* **2011**, *261*, 19–29. [CrossRef]

37. Leckie, D.G.; Ranson, K.J. Forestry applications using imaging radar. In *Principles & Applications of Imaging Radar. Manual of Remote Sensing*; Henderson, F.M., Lewis, A.J., Eds.; John Wiley and Sons: Hoboken, NJ, USA, 1996; pp. 435–509.
38. SAWS. *South African Weather Service Rainfall Data 2006 to 2010*; South African Weather Service: Pretoria, South Africa, 2015.
39. SANParks. *South African National Parks Rainfall Data 2006 to 2010*; South African National Parks: Skukuza, South Africa, 2015.
40. R Development Core Team. *R: A Language and Environment for Statistical Computing*; R Foundation for Statistical Computing: Vienna, Austria, 2016.
41. Pickett, S.T.A.; Cadenasso, M.L.; Benning, T.L. Biotic and abiotic variability as key determinants of savanna heterogeneity at multiple spatio-temporal scales. In *The Kruger Experience: Ecology and Management of Savanna Heterogeneity*; du Toit, J.T., Biggs, H.C., Rogers, K.H., Eds.; Island Press: Washington, DC, USA, 2003; pp. 22–40.
42. Breiman, L.; Friedman, J.; Stone, C.J.; Olshen, R.A. *Classification and Regression Trees*; The Wadsworth and Brooks-Cole Statistics-Probability Series; Taylor & Francis: Burlington, MA, USA, 1984.
43. Naidoo, L.; Mathieu, R.; Main, R.; Kleynhans, W.; Wessels, K.; Asner, G.P.; Leblon, B. The assessment of data mining algorithms for modelling Savannah Woody cover using multi-frequency (X-, C- and L-band) synthetic aperture radar (SAR) datasets. *IEEE Geosci. Remote Sens. Symp.* **2014**. [CrossRef]
44. Wessels, K.J.; Colgan, M.S.; Erasmus, B.F.N.; Asner, G.P.; Twine, W.C.; Mathieu, R.; van Aardt, J.A.N.; Fisher, J.T.; Smit, I.P.J. Unsustainable fuelwood extraction from South African savannas. *Environ. Res. Lett.* **2013**, *8*, 1–10. [CrossRef]
45. Chauhan, N.S.; Lang, R.H.; Ranson, K.J. Radar modeling of a boreal forest. *IEEE Trans. Geosci. Remote Sens.* **1991**, *29*, 627–638. [CrossRef]
46. Bucini, G.; Hanan, N.P.; Boone, R.B.; Smit, I.P.J.; Saatchi, S.S.; Lefsky, M.A.; Asner, G.P. Woody fractional cover in Kruger National Park, South Africa. In *Ecosystem Function in Savannas*; CRC Press: Boca Raton, FL, USA, 2010; pp. 219–237.